PHYSICAL REVIEW B, VOLUME 65, 235323

Three-dimensional analysis of the electronic structure of cylindrical vertical quantum dots

Philippe Matagne and Jean-Pierre Leburton
Beckman Institute for Advanced Science & Technology and Department of Electrical and Computer Engineering,
University of Illinois at Urbana-Champaign, Urbana, Illinois 61801

(Received 5 March 2001; revised manuscript received 5 February 2002; published 18 June 2002)

We present a detailed analysis of single-electron charging effects in cylindrical vertical quantum dots (CVQD's). Emphasis is placed on three-dimensional (3D) device effects that induce appreciable features in the quantized electron spectrum and in the addition energy spectrum of CVQD's. A potential model based on a 3D analytical solution of the Poisson equation provides intuitive physical insight into the variation of the eigenspectrum as a function of the potential nonparabolicity. This analytical model is in good qualitative agreement with a full 3D self-consistent quantum simulation of single-electron charging in quantized CVQD's based on the density-functional theory. Hence we show that the spin sequences realized in filling the third and fourth electronic shells are a sensitive function of the potential nonparabolicity arising from the 3D CVQD geometry, and varying with applied gate bias. Within this ''atomic shell'' model, the addition energy spectrum reflects the influence of 3D device effects and is not necessarily a signature of a particular spin-filling sequence.

DOI: 10.1103/PhysRevB.65.235323 PACS number(s): 73.21.−b, 72.20.My, 73.40.Gk

I. INTRODUCTION

Recent experiments on single-electron charging effects in cylindrical vertical quantum dots (CVQD's) have suggested the existence of atomiclike properties of the confined electrons such as orbital motion, three-dimensional energy quantization, shell structure, and even Hund's rule.[1–4] For these reasons, CVQD's are often called ''artificial atoms.''[4–9] However, while in real atoms the confining potential arising from the nucleus charge is characterized by a central symmetry, and varies as the inverse of the distance from the center, in ''artificial atoms'' the potential is strongly confined in the vertical direction, while it is much weaker in the perpendicular plane with a quasiharmonic profile. For this reason, the two-dimensional (2D) harmonic oscillator model has often been used for interpreting, with relative success, the 2D atomiclike features observed in experiments.[1–4,10–14] However, the 2D harmonic oscillator model is an ideal picture, that suffers from significant shortcomings such as an overestimation of the electron localization in the quantum dot (QD),[15] and the perfect level degeneracy within 2D shells, which is different from experimental observations.[1–4]

In this paper, we study the deviations of this approach by considering 3D effects introduced by the real device configuration that includes (i) the influence of the doping in the lead reservoirs, (ii) the effect of depletion in the vertical direction with applied bias, and (iii) the effect of gate length on the confining potential in the quantum well. All these effects have a significant influence on the single-particle eigenlevels and the addition energy spectrum of the CVQD's. Specifically, we show that the confining potential of a real device is not purely parabolic. Consequently, the eigenlevels within a shell are no longer degenerate, which affects the charging sequence of the dot. For this purpose, we use two different approaches. We model the device by considering a cylindrical classical charge distribution resulting from the doping and the layered structure around the CVQD for which we analytically solve the 3D Poisson equation within appropriate boundary conditions. From these analytical considerations, we derive a more realistic 2D potential for the CVQD, and perform a perturbation analysis of the Hamiltonian of a 2D circular oscillator. This approach provides physical insight into the CVQD spectrum and enables us to derive general properties, independent of simulation results. However, this model is of limited application for quantitative comparison with experiments. In order to gain accuracy in our approach, we carry out a comprehensive computer simulation of the CVQD by taking into account the full device structure, the effect of the equipotential, and many-body interactions. We use the finite element solutions of coupled Poisson and Schrödinger 3D equations within the density-functional theory, suitable to simulate an arbitrary number of electrons in the CVQD.

II. CYLINDRICAL VERTICAL QUANTUM DOT STRUCTURES

Figure 1(a) shows a schematic diagram of a CVQD similar to the device investigated by Austing *et al.*[16] The structure consists of an undoped 12-nm $\mathrm{In}_{0.05}\mathrm{Ga}_{0.95}\mathrm{As}$ well and undoped $\mathrm{Al}_{0.22}\mathrm{Ga}_{0.78}\mathrm{As}$ barriers of thicknesses 9 and 7.5 nm. The inclusion of indium in the well lowers the bottom of the conduction band and circumvents the drawbacks of δ-doped $\mathrm{Al}_x\mathrm{Ga}_{1-x}\mathrm{As}$ barriers of earlier devices.[17] The lead on the side of the thinner (thicker) tunnel barrier is made of n^+GaAs and is referred to as the *source* (*drain*). The difference in the barrier thickness is required to facilitate an accumulation of electrons in the dot when the device operates in the nonlinear regime, i.e., at a large drain-source bias. In this paper, however, we will exclusively focus on a regime close to equilibrium so that the electronic structure of the QD is unaffected by the drain-source bias. The doping is gradually reduced from $N_D = 2\,10^{18}/\mathrm{cm}^3$ at the source (drain) to $N_D = 10^{17}/\mathrm{cm}^3$ at the double-barrier heterostructure (DBH) over a distance of 4000 Å. The DBH is etched to form a circular mesa with a geometrical diameter of the top contact of

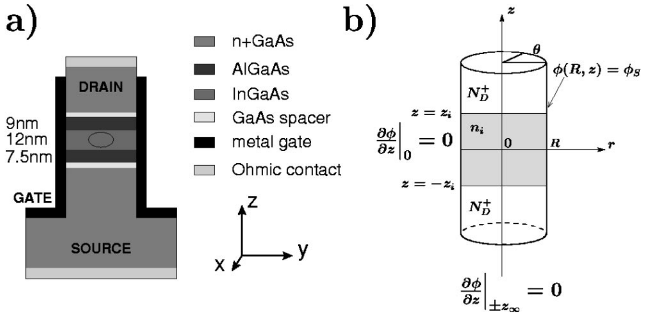

FIG. 1. (a) Schematic diagram of a cylindrical vertical quantum dot tunneling heterostructure showing the different semiconductor layers. The quantum dot, represented by the oval, lies in a 12-nm-wide quantum well ($\mathrm{In}_{0.05}\mathrm{Ga}_{0.95}\mathrm{As}$) surrounded by two potential barriers ($\mathrm{Al}_{0.22}\mathrm{Ga}_{0.78}\mathrm{As}$) whose thicknesses are 7.5 nm on the source side and 9 nm on the drain side. (b) Cylindrical charge model for the CVQD structure with boundary conditions. N_D^+ is the ionized donor concentration, and (r,θ,z) are the cylindrical coordinates.

0.5 μm. A circular Schottky gate surrounding the mesa controls the number of electrons in the dot.

III. ANALYTICAL MODEL

In order to investigate the effect of 3D geometry on the confining potential in the dot and describe its deviations from parabolicity, we model the CVQD as a cylindrical structure [Fig. 1(b)] by taking into account macroscopic parameters such as the doping of the source and the drain (N_D), the radius of the device (R), the pinning of the conduction band at the Schottky gate interface (ϕ_S), and the well width ($2z_i$), and include the effect of the third dimension.

A. Potential model

The model consists of an intrinsic region for $-z_i \leqslant z \leqslant z_i$ surrounded by two depleted regions for $|z|>|z_i|$, which extends up to $z=\pm z_\infty$ where it becomes neutral. The structure is assumed to be symmetric around $z=0$, and the potential $\phi=\phi(r,z)$ does not depend on θ. The dot is also assumed to be empty of electrons in order to capture only the structural effects, as opposed to the many-body effects due to electron-electron interactions on the confining potential. We obtain the confining potential ϕ by solving the 3D Poisson equation

$$\frac{\partial^2\phi}{\partial r^2}+\frac{1}{r}\frac{\partial\phi}{\partial r}+\frac{1}{r^2}\frac{\partial^2\phi}{\partial\theta^2}+\frac{\partial^2\phi}{\partial z^2}=-\frac{\rho}{\epsilon}, \tag{1}$$

where ρ is a charge density such as

$$\rho=0 \quad (-z_i<z<z_i)$$

and

$$\rho=qN_D^+ \quad (|z|>z_i)\,.$$

Here ϵ is the dielectric constant. Since $z_{\pm\infty}\approx 300$ Å is much smaller than the source (drain)-DBH distance (4000 Å), the doping variation is neglected in the analytical model. The boundary conditions at $z=\pm z_\infty$ are such as the z field is relaxed, i.e., $(\partial\phi/\partial z)|_{\pm z_\infty}=0$, and $\phi_S=\phi(R,z)$ is the Schottky barrier potential at the gate interface ($r=R$).

1. Intrinsic region $(0\leqslant z\leqslant z_i)$

We separate variables to solve Eq. (1), and find, for the potential,[18]

$$\phi(r,z)=\phi_S+\sum_n A_n J_0(\gamma_n r)(e^{-\gamma_n z}+e^{\gamma_n z}), \tag{2}$$

where $\gamma_n=\mu_n/R$ and μ_j is the jth zero of the zero-order Bessel function of the first kind J_0.

2. N-doped region $(z>z_i)$

By using the same technique as above, we find

$$\phi(r,z)=\phi_S-K(R^2-r^2)+\sum_n B_n J_0(\gamma_n r)e^{\gamma_n z_\infty}(e^{-\gamma_n(z-z_\infty)}+e^{\gamma_n(z-z_\infty)}), \tag{3}$$

where $K=qN_D^+/4\epsilon$. The constants A_n and B_n are determined by matching the values ϕ and $\partial\phi/\partial z$ at $z=z_i$, which yields

$$A_p=\frac{2KR^2}{\mu_n^2}\,\frac{J_2(\mu_n)}{J_1^2(\mu_p)}\,\frac{\sinh[\gamma_p(z_\infty-z_i)]}{\sinh[\gamma_p z_\infty]} \tag{4}$$

and

$$B_p=\frac{-2KR^2e^{-\gamma_p z_\infty}}{\mu_n^2}\,\frac{J_2(\mu_n)}{J_1^2(\mu_p)}\,\frac{\sinh[\gamma_p z_i]}{\sinh[\gamma_p z_\infty]} \tag{5}$$

so that the potential inside the dot can be rewritten as

$$\phi(r,z)=\phi_s-\frac{qN_D^+R^2}{\epsilon}\sum_{n=0}\frac{\sinh[\gamma_n(z_\infty-z_i)]}{\sinh(\gamma_n z_\infty)}\times\frac{J_2(\mu_n)}{\mu_n^2J_1^2(\mu_n)}J_0(\gamma_n r)ch(\gamma_n z). \tag{6}$$

By taking the limit $z\rightarrow 0$ in Eq. (6), we obtain the potential in the center of the dot. We make use of the power expansion of $J_0(x)$ and invert the summations to obtain the following expression:

$$\phi(r)=\phi_0-\alpha\frac{qN_D^+}{4\epsilon}r^2-\Lambda\left(\frac{r}{R}\right)r^4. \tag{7}$$

If we denote

$$C_n=\frac{\sinh[\gamma_n(z_\infty-z_i)]}{\sinh(\gamma_n z_\infty)}\,\frac{J_2(\mu_n)}{J_1^2(\mu_n)}, \tag{8}$$

which is simply a structure factor depending on the problem geometry, the first term

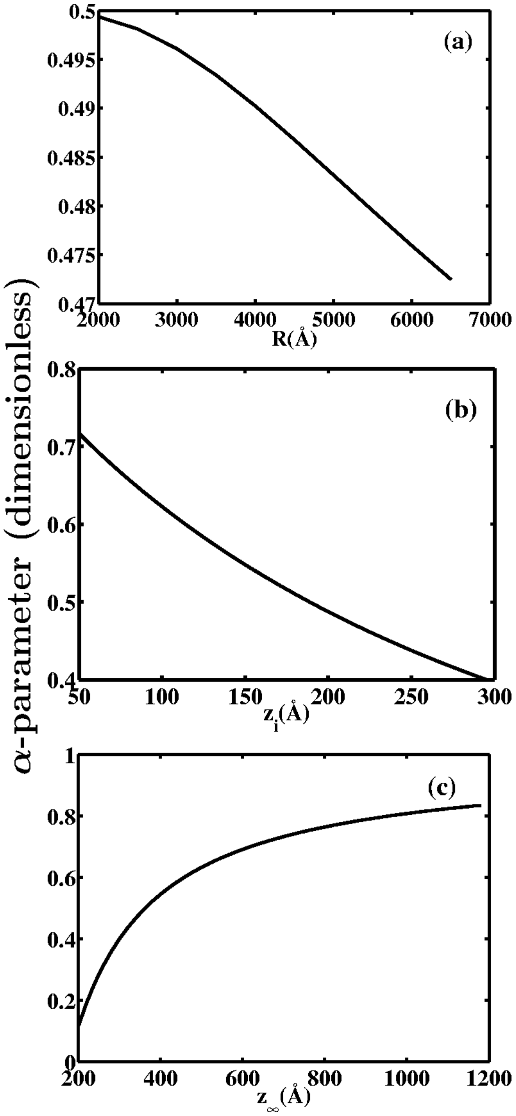

FIG. 2. Variation of the form factor α as a function of (a) the dot radius R, ($z_i = 175$ Å, $z_\infty \approx 350$ Å), (b) the well width $2z_i$ ($R = 2500$ Å, $z_\infty \approx 350$ Å), and (c) the extension of the depletion width z_∞ ($R = 2500$ Å, $z_i = 175$ Å) in the vertical direction.

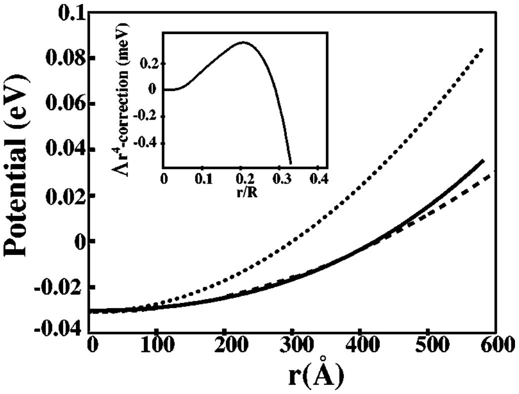

FIG. 3. Comparison between the profiles of the conduction band edge ($z = 0$) computed from self-consistent simulations (solid) and from our 3D cylindrical charge model (dashed). The dotted curve shows a parabolic potential with $K = qN_D/4\epsilon$. The inset shows the Λr^4 correction to the harmonic potential as a function of r/R, where R is the dot radius.

$$\phi_0(V_G,N_D^+) = \phi_S(V_G) - \frac{qN_D^+R^2}{\epsilon}\sum_n \frac{C_n}{\mu_n^2} \tag{9}$$

represents the potential in the bottom of the dot which depends on the applied gate voltage V_G. The second term is the harmonic term with the form factor $\alpha = \Sigma_n C_n$. We note that this term does not scale directly with the dot radius R, nor with V_G. However, there is a hidden dependence on these factors through the α parameter that is a function of R, z_i and z_∞, as shown on Fig. 2. Our model predicts a weak dependence on the radius of the structure R [Fig. 2(a)] but a strong dependence on z_i and z_∞ [Figs. 2(b) and 2(c)]. In plotting the R dependence of the α factor, we use $z_i = 175$ Å, according to device geometry, and $z_\infty \approx 350$ Å, that is is extracted from the solution of our numerical model presented here after. The weak dependence on R is not surprising since the solution of the 2D harmonic oscillator is only a function of the doping level. The z_i dependence can be understood by noting that, by increasing the width of the intrinsic ($\rho = 0$) well, the field density, and thus the potential curvature in the longitudinal direction (z), decrease. In Fig. 2(b), we use $R = 2500$ Å, and we keep the depleted region $z_\infty - z_i$ constant at 200 Å in order to maintain the charge constant. The z_∞ dependence of α (here $R = 2500$ Å and $z_i = 175$ Å) is strong because the variation of z_∞ implies a significant change in the charge of the depleted region, which, via the Poisson equation, results in a strong variation of the electrostatic potential curvature. It is worth emphasizing that Fig. 2(c) reflects the 3D nature of the potential variation, with correlation between its curvature along the radial and longitudinal directions. Figure 3 shows that the 2D harmonic oscillator (dotted curve) model, with a spring constant $K = qN_D^+/4\epsilon$, overestimates the real potential curvature compared with 3D models. This is consistent with the z_i dependence of the α factor previously obtained since the 2D harmonic-oscillator picture can be considered as the limit for $z_i \rightarrow 0$ of the 3D problem [Fig. 2(b)]. In practical problems, K is a fitting parameter[19,20] fudged with a power variation of n, the electron density, but then it loses its physical meaning since it is unrelated to any of the nanostructure parameters.

The last term in Eq. (7) is the 3D correction to the "quasi-2D" parabolic potential with

$$\Lambda\left(\frac{r}{R}\right) = \frac{qN_D^+}{4\epsilon R^2}\sum_{n=0}^{\infty} C_n \sum_{l=0}^{\infty} (-1)^{l+1}\frac{\mu_n^{2l+2}}{2^{2l+2}[(l+2)!]^2}\left(\frac{r}{R}\right)^{2l}. \tag{10}$$

We point out that, while retaining the cylindrical symmetry, this term is structure (N_D^+, C_n) and geometry (R) dependent; it is not necessarily negligible, grows with r/R, and could be positive or negative since J_2 oscillates with μ_n. The correction Λr^4 is plotted as a function of (r/R) in the inset of Fig. 3. It is seen that the correction is small but not negligible at a short distance from the origin.

B. 2D eigenstates analysis

Since the effective dot radius is much smaller than R, the Λr^4 correction can be treated as a perturbation of a parabolic potential in the quantum-mechanical problem of the determination of the eigenvalues and the eigenfunctions in the QD.[21] Hence we consider the actual xy potential profile to be given by

$$\phi(r,\theta)=\phi_{osc}(r)+W(r,\theta), \tag{11}$$

where $\phi_{osc}(r)=\phi_0-Kr^2$ is the harmonic potential of Eq. (7), and W is a perturbation which contains the Λ correction term and, for the sake of generality, depends on r and θ [Fig. 1(b)]. If the confining potential ϕ retains cylindrical symmetry, one can state the following

(1) ϕ commutes with the two-dimensional angular momentum operator $(\hbar/i)(\partial/\partial\theta)$. Therefore, H and H_0 have the same eigenfunctions $\varphi_{n_r,M}$.

(2) $\varphi_{n_r,M}$ and $\varphi_{n_r,-M}$ can be generated from one another by rotation, i.e., if $\boldsymbol{R}$ is a rotation operator with a z axis, $\boldsymbol{R}\varphi_{n_r,-M}=\varphi_{n_r,M}$. Therefore, $\varphi_{n_r,M}$ and $\varphi_{n_r,-M}$ have the same energy: $\varepsilon_{n_r,|M|}$.

Thus, as long as the perturbation is small with respect to $\hbar\omega$, the shell structure in CVQD's is preserved. However, within a shell, degeneracy is partially lifted, and subshell levels, characterized by identical absolute values in their quantum number M, emerge.

When the cylindrical symmetry is broken, by, for instance, the electron occupation of non-s orbitals, deviations from the circular shape of the dot and/or potential fluctuations arising from the long-range Coulomb interaction of ionized donors in GaAs, the eigenlevels are, in general, no longer degenerate. We illustrate the consequences of broken spatial symmetry by two examples of perturbations. Since the cylindrical symmetry is not preserved, quantum numbers (n_r,M) are, in general, no longer appropriate, although, as shown on Fig. 4, the eigenfunctions may, in some cases, retain strong cylindrical symmetry features. To characterize the perturbed eigenfunctions and eigenvalues, we use ψ_i^k and ε_i^k, where i is the shell number and k is the appearance order within a shell. In the perturbation analysis, the ψ_n^k's will be expanded on the φ_{n_x,n_y} basis.

1. $qW=\lambda\hbar\omega\mathcal{X}\mathcal{Y}$

Here, $\mathcal{X}$ and $\mathcal{Y}$ are the position operators along the x and y directions, respectively. This perturbation arises, for example, from the electron charge due to the occupation of a p orbital, present in every shell. Expressing the operators $\mathcal{X}$ and $\mathcal{Y}$ in terms of the annihilation $\boldsymbol{a}$ and creation $\boldsymbol{a}^\dagger$ operators, we find

$$q\boldsymbol{W}=\frac{\lambda\hbar\omega}{2}(\boldsymbol{a}_x^\dagger\boldsymbol{a}_y^\dagger+\boldsymbol{a}_x^\dagger\boldsymbol{a}_y+\boldsymbol{a}_x\boldsymbol{a}_y^\dagger+\boldsymbol{a}_x\boldsymbol{a}_y). \tag{12}$$

The perturbation matrix in the $j+1$ harmonic oscillator eigenfunction basis (n_x,n_y) reads

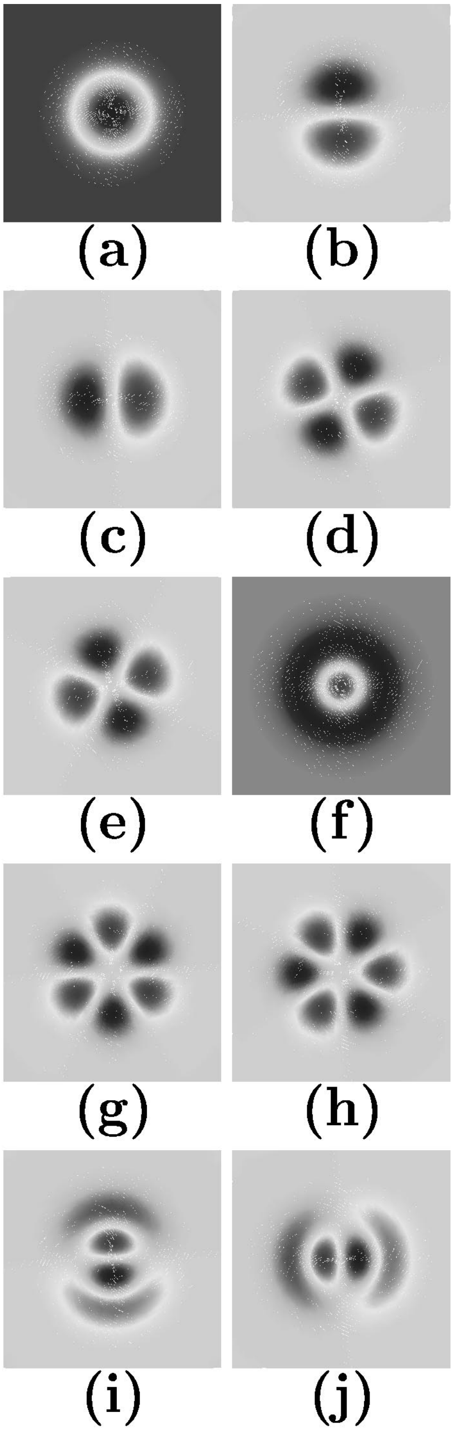

FIG. 4. Wave-function contourplots for the four first shells of a CVQD. (a) The first shell is nondegenerate and made up of an s state ψ_0. (b) and (c) Degenerate p-like states $\psi_1^{1,2}$ belonging to the second shell. (d)–(f) Third-shell wave functions consisting of two d-like states $\psi_2^{1,2}$ [(d) and (e)] and an s-like state ψ_2^3 (f). (g)–(j) Fourth shell composed of one d-like subshell $\psi_3^{1,2}$ [(g) and (h)] and one p-like subshell $\psi_3^{3,4}$ [(i) and (j)].

TABLE I. Terms of the expansion of $(\mathcal{X}^2\mathcal{Y}^2)$ in term of $\boldsymbol{a}^\dagger$ and $\boldsymbol{a}$ operators.

Term	Effect on n_x	Effect on n_y	Effect on state
$\boldsymbol{a}_x^2\boldsymbol{a}_y^2$	-2	-2	none
$\boldsymbol{a}_x^2[2N_y+1)]$	-2	0	none
$\boldsymbol{a}_x^2\boldsymbol{a}_y^{\dagger\,2}$	-2	$+2$	third shell and following
$(2N_x+1)\boldsymbol{a}_y^2$	0	-2	none
$(2N_x+1)(2N_y+1)$	0	0	all
$\boldsymbol{a}_x^{\dagger\,2}\boldsymbol{a}_y^2$	$+2$	-2	third shell and following
$\boldsymbol{a}_x^{\dagger\,2}(2N_y+1)$	$+2$	0	none
$\boldsymbol{a}_x^{\dagger\,2}\boldsymbol{a}_y^{\dagger\,2}$	$+2$	$+2$	none

$$\begin{pmatrix} 0 & \sqrt{j} & 0 & \dots & & & 0 \\ \sqrt{j} & 0 & \sqrt{(j-1)2} & 0 & \dots & & 0 \\ \dots & \dots & \dots & \dots & \dots & \dots & \dots \\ 0 & \dots & & & \sqrt{2(j-1)} & 0 & \sqrt{j} \\ 0 & \dots & & & 0 & \sqrt{j} & 0 \end{pmatrix}.$$

This matrix has $j+1$ distinct eigenvalues $\pm j$, $\pm(j-2)$, $\pm(j-3)$ . . . . Thus a $\mathcal{X}\mathcal{Y}$ perturbation completely removes the degeneracy in all the shells.

2. $qW=(\hbar\omega)^2[\nu(\mathcal{X}^4+\mathcal{Y}^4)+\eta\mathcal{X}^2\mathcal{Y}^2]$

This perturbation arises from deviation from the circular shape of the dot, or from a 3D geometry such as the Λr^4-correction in Eq. (7) ($\eta=2\nu$), for instance. The details of the expansion of this perturbation in terms of the $\boldsymbol{a}^\dagger$ and $\boldsymbol{a}$ operators are gathered in the first column of Tables I and II. As shown on the second and third columns, the coefficients either raise, lower, or maintain unchanged the quantum numbers n_x and n_y. Only contributions that conserve the total quantum number n can affect the shell. We examine the effect of this perturbation on the second, third, and fourth shells, respectively.

TABLE II. Terms of the expansion of $(\mathcal{X}^4+\mathcal{Y}^4)$ in term of $\boldsymbol{a}^\dagger$ and $\boldsymbol{a}$ operators.

Term	Effect on n_x	Effect on n_y	Perturbed states
$\boldsymbol{a}_x^4$	-4	0	none
$\boldsymbol{a}_y^4$	0	-4	none
$2\boldsymbol{a}_x^2(2N_x+1)$	-2	0	none
$2\boldsymbol{a}_y^2(2N_y+1)$	0	-2	none
$\boldsymbol{a}_x^2\boldsymbol{a}_x^{\dagger\,2}$	0	0	all
$\boldsymbol{a}_y^2\boldsymbol{a}_y^{\dagger\,2}$	0	0	all
$(2N_x+1)^2$	0	0	all
$(2N_y+1)^2$	0	0	all
$2(2N_x+1)\boldsymbol{a}_x^{\dagger\,2}$	$+2$	0	none
$2(2N_y+1)\boldsymbol{a}_y^{\dagger\,2}$	0	$+2$	none
$\boldsymbol{a}_x^{\dagger\,2}\boldsymbol{a}_x^2$	0	0	third shell and following
$\boldsymbol{a}_y^{\dagger\,2}\boldsymbol{a}_y^2$	0	0	third shell and following
$\boldsymbol{a}_x^{\dagger\,4}$	$+4$	0	none
$\boldsymbol{a}_y^{\dagger\,4}$	0	$+4$	none

Second shell. The unperturbed second shell is made up of two p states φ_{01} and φ_{10}. Expanding the perturbed wave function ψ_1 on the $\{\varphi_{01},\varphi_{10}\}$ basis, we obtain

$$\left(\frac{\hbar\omega}{2}\right)^2\begin{pmatrix} 18\nu+3\eta & 0 \\ 0 & 18\nu+3\eta \end{pmatrix}\begin{pmatrix} \langle\varphi_{01}|\psi_1\rangle \\ \langle\varphi_{10}|\psi_1\rangle \end{pmatrix} = \delta\varepsilon_1\begin{pmatrix} \langle\varphi_{01}|\psi_1\rangle \\ \langle\varphi_{10}|\psi_1\rangle \end{pmatrix}. \tag{13}$$

As predicted, the p states [Figs. 4(b) and 4(c)] remain degenerate. Nevertheless, they are shifted by

$$\delta\varepsilon_1=(18\nu+3\eta)\left(\frac{\hbar\omega}{2}\right)^2. \tag{14}$$

Consequently, the W perturbation in this section does not affect the 2D shell. Only deviations from cylindrical symmetry lift the degeneracy of this shell.

Third shell. The unperturbed third shell consists of three degenerate states φ_{11}, φ_{01}, and φ_{20}. Expanding the perturbed wave function ψ_2 on the $\{\varphi_{02},\varphi_{11},\varphi_{20}\}$ basis, we find

$$\left(\frac{\hbar\omega}{2}\right)^2\begin{pmatrix} 42\nu+5\eta & 0 & 2\eta \\ 0 & 30\nu+9\eta & 0 \\ 2\eta & 0 & 42\nu+5\eta \end{pmatrix}\begin{pmatrix} \langle\varphi_{02}|\psi_2\rangle \\ \langle\varphi_{11}|\psi_2\rangle \\ \langle\varphi_{20}|\psi_2\rangle \end{pmatrix} = \delta\varepsilon_2\begin{pmatrix} \langle\varphi_{02}|\psi_2\rangle \\ \langle\varphi_{11}|\psi_2\rangle \\ \langle\varphi_{20}|\psi_2\rangle \end{pmatrix}, \tag{15}$$

with the following solutions:

$$\delta\varepsilon_2^1=\left(\frac{\hbar\omega}{2}\right)^2(42\nu+3\eta),\quad |\psi_2^1\rangle=\frac{1}{\sqrt{2}}(|\varphi_{02}\rangle-|\varphi_{20}\rangle)$$

$$\delta\varepsilon_2^2=\left(\frac{\hbar\omega}{2}\right)^2(30\nu+9\eta),\quad |\psi_2^2\rangle=|\varphi_{11}\rangle \tag{16}$$

$$\delta\varepsilon_2^3=\left(\frac{\hbar\omega}{2}\right)^2(42\nu+7\eta),\quad |\psi_2^3\rangle=\frac{1}{\sqrt{2}}(|\varphi_{02}\rangle+|\varphi_{20}\rangle).$$

The perturbed third shell [Figs. 4(d), 4(e), and 4(f)] now is made up of one s state (ψ_2^3) and one d state (ψ_2^1), that are linear combinations of two unperturbed states and one d state (ψ_2^2) identical to φ_{11}. In general, the threefold degeneracy is completely lifted. It is worth noting that, even in the pure radial case, i.e., $\eta=2\nu$, which is the situation described by the Λr^4 correction seen in Eq. (7) of our analytical model, the degeneracy is partially lifted, i.e., as explained above, the accidental degeneracy between the $s[(n_r,M)=(1,0)]$ and p $[(n_r,M)=(0,\pm2)]$ states is lifted. Thus, *even when the dot is empty*, we do not expect the third shell to remain degenerate, as opposed to the prediction of the 2D harmonic-

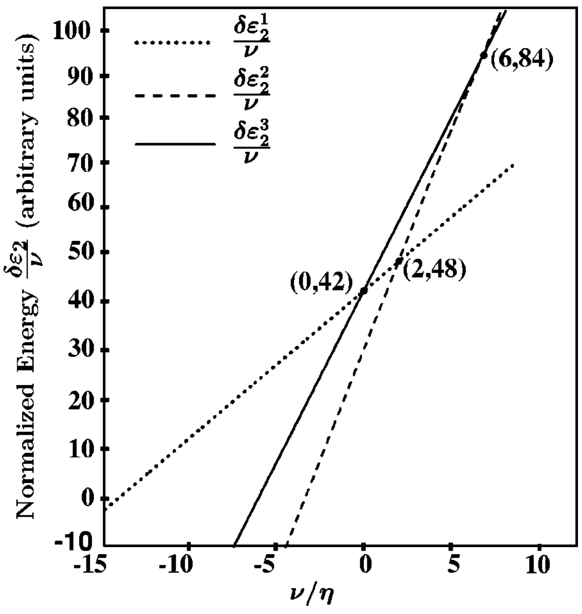

FIG. 5. Variation of the normalized perturbations of single-particle eigenlevels of the third shell $\delta\varepsilon_2^1/\nu$ (dotted), $\delta\varepsilon_2^2/\nu$ (dashed), $\delta\varepsilon_2^3/\nu$ (solid) as a function of ν/η. The crossing point as function of horizontal and vertical coordinates shows an inversion of the state ordering sequence.

oscillator model. Figure 5 shows a plot of $\delta\varepsilon_2^1$, $\delta\varepsilon_2^2$, and $\delta\varepsilon_2^3$ as a function of η/ν. It is seen that the third level is very sensitive to the perturbation and, depending on the sign and magnitude of ν and η, can result in any ordering state sequence. Perturbations due to the electron occupancy of non-*s* orbitals or weak elliptic deviations of the geometry result in $\nu>0$ and $2<\eta<3$, i.e., the degeneracy between the two *d* states is slightly lifted and the *s* state is higher in energy. A completely different situation would occur when a donor impurity is placed close to the center of the dot. Then, the $1/r$ hydrogenic potential changes the curvature in the bottom of the dot, yielding $\nu<0$ and $-3<\eta<-2$, so that the *s* state is now below the two *d* states.

Fourth shell. The unperturbed fourth shell is made up of four degenerate states φ_{12}, φ_{21}, φ_{03}, and φ_{30}. Expanding the perturbed wave function ψ_3 on the $\{\varphi_{12},\varphi_{21},\varphi_{30},\varphi_{03}\}$ basis, we obtain

$$\left(\frac{\hbar\omega}{2}\right)^2\begin{pmatrix} 54\nu+15\eta & 0 & 2\sqrt{3}\,\eta & 0 \\ 0 & 54\nu+15\eta & 0 & 2\sqrt{3}\,\eta \\ 2\sqrt{3}\,\eta & 0 & 78\nu+7\,\eta & 0 \\ 0 & 2\sqrt{3}\,\eta & 0 & 78\nu+7\,\eta \end{pmatrix}$$
$$\times\begin{pmatrix} \langle\varphi_{12}|\psi_3\rangle \\ \langle\varphi_{21}|\psi_3\rangle \\ \langle\varphi_{30}|\psi_3\rangle \\ \langle\varphi_{03}|\psi_3\rangle \end{pmatrix} = \delta\varepsilon_3\begin{pmatrix} \langle\varphi_{12}|\psi_3\rangle \\ \langle\varphi_{21}|\psi_3\rangle \\ \langle\varphi_{30}|\psi_3\rangle \\ \langle\varphi_{03}|\psi_3\rangle \end{pmatrix}, \qquad (17)$$

which leads to two twofold degenerate subshells whose eigenlevels read

$$\delta\varepsilon_3^{1,2}=\left(\frac{\hbar\omega}{2}\right)^2(66\nu+11\eta\pm\sqrt{144\nu^2-96\nu\eta+28\eta^2}). \qquad (18)$$

The expression under the square root is always positive (except for the trivial case $\nu=\eta=0$) so that the two subshells never merge back. As seen in Figs. 4(g), 4(h), 4(i), and 4(j), the perturbed shell is made up of a *p*-like subshell and an *f*-like subshell. The effect of the perturbation is to lift the accidental degeneracy between the *p* and *f* states, even for an empty dot, as opposed to the 2D harmonic-oscillator model predictions.

IV. NUMERICAL MODEL

In order to test the validity of our analytical model, we perform a full scale 3D self-consistent numerical analysis of the structure. The charge density in the QD is obtained by considering the quantum-mechanical nature of the charge carriers within the density functional theory (DFT) to describe many-body effects among electrons in the dot.[22] In order to take into account the spin dependence on the electron-electron interaction, two Kohn-Sham equations, one for spin-up and one for spin-down, are solved simultaneously:

$$H^{\uparrow}(\boldsymbol{r})\psi_i^{\uparrow}(\boldsymbol{r})=\varepsilon_i^{\uparrow}\psi_i^{\uparrow}(\boldsymbol{r}), \quad H^{\downarrow}(\boldsymbol{r})\psi_i^{\downarrow}(\boldsymbol{r})=\varepsilon_i^{\downarrow}\psi_i^{\downarrow}(\boldsymbol{r}). \qquad (19)$$

Here ε_i and ψ_i are the corresponding eigenenergies and eigenstates of the Hamiltonian $H^{\uparrow}$ and $H^{\downarrow}$,

$$H^{\uparrow(\downarrow)}(\boldsymbol{r})=-\frac{\hbar^2}{2}\nabla\left[\frac{1}{m^*(\boldsymbol{r})}\nabla\right]-q\phi(\boldsymbol{r})+\Delta E_c+\phi_{xc}^{\uparrow(\downarrow)}(n), \qquad (20)$$

where $m^*(\boldsymbol{r})$ is the position-dependent effective mass. $\phi(\boldsymbol{r})=\phi_{ext}+\phi_{ion}+\phi_H$ is the electrostatic potential which consists of three contributions: ϕ_{ext} is the potential due to external applied bias, ϕ_{ion} is the potential resulting from ionized donors, and ϕ_H is the Hartree potential accounting for repulsive electron-electron interactions. ΔE_c is the conduction-band offset between different materials, i.e., 181 meV for $Al_{0.22}Ga_{0.78}As$/GaAs and 50 meV for GaAs/$In_{0.05}Ga_{0.95}As$, and $\phi_{xc}^{\uparrow(\downarrow)}$ is the exchange and correlation potential energy for spin up (↑) and down (↓) that is computed within the local-spin density approximation (LSDA) according to Perdew and Wang's formulation.[23] Hence our approach is spin unrestricted, i.e., allows for different orbitals for different spins. The LSDA approach to the study of the electronic structure of quantum dots has been well tested by many authors.[24–27] It successfully explains the quasi-two-dimensional shell structures and spin configurations of quantum dots and is in good agreement with 2D quantum Monte Carlo (QMC) simulations.[12,13,28] Moreover, applications of the LSDA to few-electron atoms have shown accuracies of the order of 1% in the calculations of the atoms ionization energy.[22]

The electron density in the QD reads

$$n(\boldsymbol{r}) = n^{\uparrow}(\boldsymbol{r}) + n^{\downarrow}(\boldsymbol{r}) = \sum_{i=1}^{N_{\uparrow}} |\psi_i^{\uparrow}(r)|^2 + \sum_{i=1}^{N_{\downarrow}} |\psi_i^{\downarrow}(r)|^2, \quad (21)$$

where $N_{\uparrow} + N_{\downarrow} = N$ is the number of electrons in the dot.

The electrostatic potential $\phi(\boldsymbol{r})$ is computed by solving Poisson's equation,

$$\nabla[\epsilon(\boldsymbol{r})\nabla\phi(\boldsymbol{r})] = -\rho(\boldsymbol{r}), \quad (22)$$

where $\epsilon(\boldsymbol{r})$ is the position-dependent permittivity and $\rho(\boldsymbol{r})$ is the total charge density which is given by

$$\rho(\boldsymbol{r}) = q[N_D^{+}(\boldsymbol{r}) - n(\boldsymbol{r})] \quad (23)$$

where $n(\boldsymbol{r})$ and $N_D^{+}(\boldsymbol{r})$ are the electron and ionized donors densities, respectively, at the position $\boldsymbol{r}$.

Equations (19) and (22) are discretized by the finite-element method, of which a detailed formulation has been published elsewhere.[29] The numerical formulation of both equations leads to sparse linear systems. The discretization of the Poisson equation leads to a boundary value problem for which we use a conjugate gradient approach, whereas the discretization of Kohn-Sham equations leads to a generalized eigenvalue problem. For the latter, the first eigenvalues and eigenvectors are extracted by a subspace method. Finally, the algorithm used to self-consistently couple both problems is based on the Newton-Raphson method.

Boundary conditions for the electrostatic potential ϕ are chosen by imposing Dirichlet conditions at the source, drain, and lateral surfaces of the device. At the source and drain a flatband condition is assumed, and ϕ is set up such that the net charge is zero in these regions. Along lateral surfaces, the Schottky barriers heights ϕ_s are strongly influenced by surface chemistry, so we use the experimental data of Grant *et al.*[30] and Best.[31] On the gated surfaces, the Schottky barriers are modified by $\phi_s - V_G$, where V_G is the gate bias.

Boundary conditions for the Schrödinger equation are imposed by assuming vanishing wave functions on any lateral surface of the device. Since the quantum dot is much smaller than the physical dimensions of the device, the wave functions actually vanish much before reaching those boundaries. In the direction perpendicular to the heterointerfaces, we allow the wave functions to leak into the source and drain regions. However, this leakage is very weak and is not taken into account in the computation of the charge in the source and drain regions which is entirely determined using the Thomas-Fermi approximation. This assumption is reasonable, since the weak leakage does not affect the charge in the dot, and is negligible compared to the bulk charge in the source and drain regions.

Because the quantum dot is weakly coupled to the source and drain, electrons are completely localized in the dot. At equilibrium, and for a given bias, the integer number of electrons N minimizes the total energy E_T of the dot. In order to determine N, we use the Slater formula:[32]

$$E_T(N+1) - E_T(N) = \int_0^1 \varepsilon_{LUO}(n)\,dn \approx \varepsilon_{LUO}(1/2) - E_F, \quad (24)$$

where $E_T(N)$ is the total energy for N electrons in the dot, ϵ_{LUO} is the lowest unoccupied orbital eigenvalue, and E_F is the Fermi energy. Equation (24) is based on Janak's theorem,

$$\varepsilon_i = \frac{\partial E_T}{\partial n_i}, \quad (25)$$

which assumes an incremental and continuous variation of the electron occupation n_i of level i.

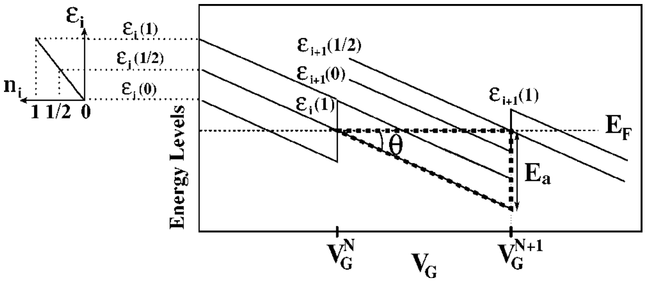

FIG. 6. Schematic of the energy spectrum in the gate voltage interval corresponding to successive charging of two electrons. The single-particle energy $\varepsilon_i(n_i)$ is represented by the level index (i) and its electron occupation n_i. E_F and E_a are the Fermi level and the addition energy, respectively. θ is the slope of the variation of the eigenlevel as a function of the gate voltage. Side: variation of the eigenlevels $\varepsilon_i(n_i)$ as a function of their occupation number n_i.

Hence, upon populating ϵ_{LUO} with 0.5 electron, a stable configuration of N electrons is achieved in the dot if $E_T(N+1) > E_T(N)$, i.e., if the integral of Eq. (24) is positive; otherwise there are $N+1$ electrons. It must be noted that the approximation made in Eq. (24) is valid only if ϵ_{LUO} varies linearly with N.[25]

The addition energy computation is based on Eq. (24). By definition,

$$E_a = E_F(N+1) - E_F(N), \quad (26)$$

$$E_F(N) = E_T(N) - E_T(N-1), \quad (27)$$

where E_a is the addition energy and E_T is the total energy. Although the term addition energy to denote E_a is somehow improper—*stricto sensu*, the addition energy, i.e., the energy required to add one electron to the dot, is the electrochemical potential[5,26]—we follow Likharev[33] and Tarucha *et al.*[1] and maintain this denomination. Using Eqs. (24), (26), and (27), we obtain

$$E_a = E_F(N+1) - E_F(N) \quad (28)$$

$$= [E_T(N+1) - E_T(N)] + [E_T(N) - E_T(N-1)] \quad (29)$$

$$= \varepsilon_{LUO}^{N}(1/2) - \varepsilon_{LUO}^{N-1}(1/2). \quad (30)$$

From Fig. 6, we have

$$E_a = (V_G^{N+1} - V_G^{N})\,tg(\theta) \quad (31)$$

if we assume that, for N electrons, $\varepsilon_{LUO} = \varepsilon_{i+1}$, and for $N-1$ electrons $\varepsilon_{LUO} = \varepsilon_i$. Here the upper script of ε gives the total number of electrons in the system, and the number between brackets gives the occupancy of a single-particle level.

Let us now assume that ε_i is a bilinear function of n_i and V_G, which, as we will see, is the case in our simulations,

$$\varepsilon_i(n_i,V_G)=an_i+bV_G+c, \tag{32}$$

where *a*, *b*, and *c* are constant coefficients to be determined. Obviously, from Slater's formula [Eq. (24)] and taking $E_F=0$ as the energy reference, we have

$$\varepsilon_i^N(n_i,V_G)=an_i+b(V_G-V_G^{N+1})-a/2. \tag{33}$$

Thus

$$\varepsilon_i^N(n_i,V_G^{N+1})=an_i-a/2 \tag{34}$$

and

$$\int_0^1 \varepsilon_i^N dn_i=\int_0^1 (an_i-a/2)dn_i=\left[\frac{an_i^2}{2}-\frac{an_i}{2}\right]_0^1=0$$
$$=\varepsilon_i^N(1/2,V_G^{i+1}), \tag{35}$$

which confirms Slater's rule. Moreover, using Eq. (34), one obtains

$$\varepsilon_i^N(1,V_G^{i+1})=a/2, \quad \varepsilon_i^N(0,V_G^{i+1})=-a/2, \tag{36}$$

as illustrated in Fig. 6. It is therefore possible to test the validity of Slater's formula by simulating the dot at $V_G=V_G^{i+1}$ and populating ε_i with 0, 1/2, and 1 electrons to check if the shift of ε_i is symmetric with respect to E_F. In our simulations, this test was systematically verified for all numbers of electrons in the dot, except $N=1$, which is beyond the validity of Janak's theorem [Eq. (25)] since then the electron variation from 0 to 1 is far from incremental.

V. RESULTS AND DISCUSSION

Figure 7 shows the single-particle eigenspectrum for the first ten orbitals in the CVQD as a function of the gate voltage V_G as obtained from the 3D computational model. Because of their spatial symmetry and spin degeneracy, the orbitals are grouped into four sets of levels which, when occupied by electrons, will form the first four shells. The upper horizontal scale indicates the number of electrons in the QD on a particular range of V_G. On the vertical scale, the Fermi level is taken as the reference at zero. Below $V_G=-0.62$ V, all levels are empty and decrease monotonically with V_G as the potential energy is lowered.

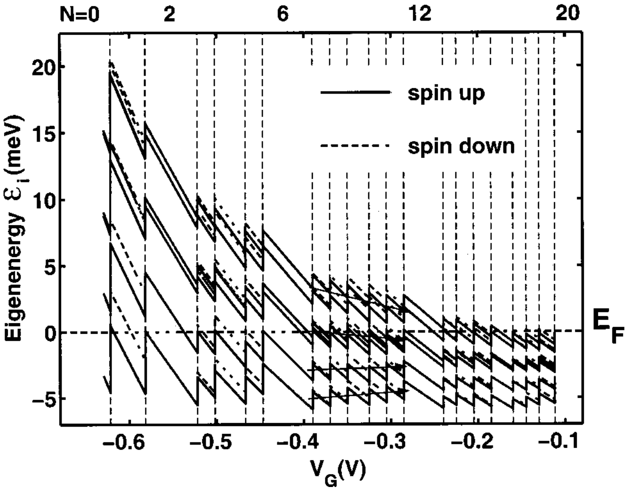

FIG. 7. Energy spectrum of the first four sets of eigenlevels (solid curves: spin-up, dotted curves: spin-down) as a function of the gate voltage V_G (bottom horizontal axis) and number of electrons *N* (top horizontal axis). E_F is the Fermi level.

The variation of all eigenlevels ε_i are piecewise linear with respect to V_G. At each transition from *N* to $N+1$ electrons, each curve $\varepsilon_i(V_G)$ is discontinuous with an upward shift. This is a manifestation of the Coulomb blockade effect: when a new electron enters the dot, it induces an upward shift of the whole spectrum because of the sudden increase of the total electrostatic energy in the dot due to Coulomb interaction. Here the first electron entering the dot occurs for $V_G=-0.62$ V. It must be noted that, the higher the shell being populated, the smaller the shifts, i.e., the smaller the charge increment. Unlike in orthodox Coulomb blockade experiments,[34] ΔV_G, the voltage increment for adding an electron in the dot, takes very unequal values, irregularly distributed over the range of V_G, because of the influence of the quantization and quantum many-body effects during the charging of the dot. ΔV_G is large for $N=2$, 6, and 12, i.e., after the complete filling of each shell because, in addition to the energy required to overcome the electrostatic repulsion of the electrons already present in the dot, an energy contribution is needed to lower the next orbital below the Fermi level for admitting the next electron.

We note that in the interval between the addition of two electrons, $\varepsilon_i(V_G)$ decreases monotonically with V_G because the overall potential energy of the system decreases as the gate voltage is made more positive. This behavior is different from the results of Nagaraja *et al.*,[35] whose model did not account for individual spin states. In that case, the single-particle eigenvalues were tangential to the Fermi level during the charging of the whole orbital.

During the charging process over the whole gate voltage range ($-0.62\ \text{V}<V_G<-0.082\ \text{V}$), the four sets of levels (shells) remain well separated, which indicates that the shell structure is preserved. However, as predicted by the analytical model, the degeneracy of levels belonging to the same shell, even when nonoccupied, i.e., second, third, and fourth sets of levels for $-0.522\ \text{V}<V_G<-0.447\ \text{V}$, are partially lifted.

Another interesting feature appears by considering the overall energy variation of the different shells during a single shell charging. For instance, for $-0.39\ \text{V}<V_G<-0.285\ \text{V}$, i.e., during the third shell charging, the average energy of the two lower full shells is higher at the end of the charging process than at the beginning. This is easily seen by drawing a line joining the middle of each discontinuity segment. For the two lower shells, the slope is positive, which indicates an overall energy repulsion among these shells. For the third filling shell, the slope is slightly negative, which means that the attractive energy of the gate field

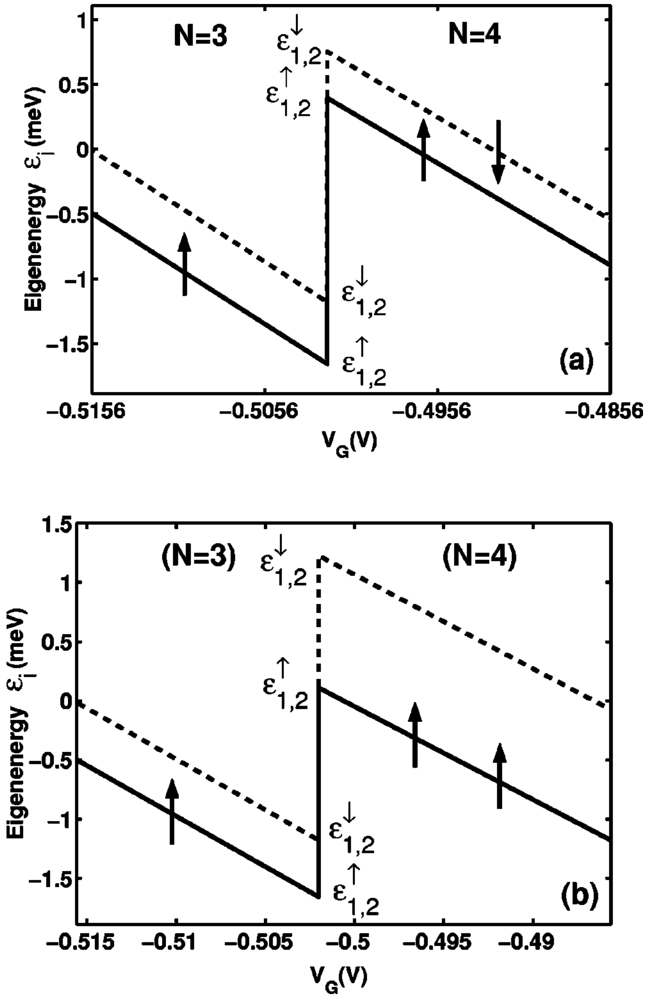

FIG. 8. Single-particle energy spectrum three possible configurations (a), (b), and (c) around the $N=3\rightarrow4$ transition in the second shell (dashed: spin-down; solid: spin-up). The insets show the two *p* orbitals with the spin position and direction. For $N=3$, the single electron sits on the second lower state.

is just sufficient to overcome the electron repulsion energy. Finally, for the upper empty shell, the slope is negative because, free of electron repulsion, the eigenstates only experience the attractive effect of the gate.

We also notice the decrease of the intershell energy separation as V_G increases, as observed experimentally.[1] This effect is generally interpreted as due to the Coulomb interaction between high-energy electrons with extended wave functions which weakens the confining potential. However, our analytical model reveals that, in CVQD's, there is in addition a pure *3D geometrical effect* that enhances the level collapse when V_G increases *even if the dot is empty*. Indeed, from Eq. (8), the quadratic term α in the potential depends on the depletion region extension z_∞. As z_∞ decreases when V_G is made more positive, so does α (Fig. 2). Therefore, as V_G is swept, we expect the oscillator frequency to decrease and, thereby, the shell separation. This effect is at the origin of the renormalization of the harmonic-oscillator frequency by the fourth root of the electron density, i.e., $\omega\propto 1/n^{1/4}$, in models based on pure 2D parabolic confining potential.[19,20]

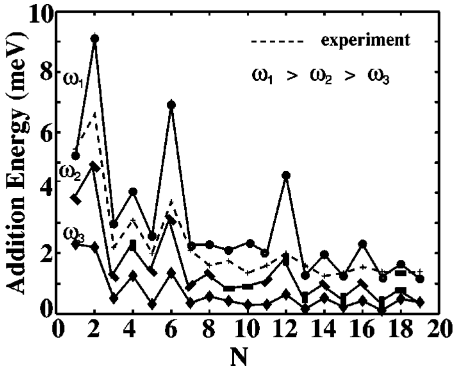

FIG. 9. Comparison between computed addition energy spectra (solid) for three different confining potentials $\omega_1>\omega_2>\omega_3$ and the experimental spectrum (Ref. 1) (dashed) as a function of the number of electrons. Note that, by definition, $E_a(N)=E_F(N+1)-E_F(N)$, so that a value for $N=j$ in this figure refers to the energy needed to add the $(j+1)$th electron in the dot.

This $n^{-1/4}$ renormalization was justified to maintain the electron concentration constant during charging of the dot, which is readily obtained in our simulations.

During the filling of a particular shell, e.g., the second shell (-0.522 V$<V_G<-0.447$ V), the eigenlevel ordering within a shell is determined by Coulomb repulsion resulting from wave-function overlap and exchange and correlation effects that favor electrons with parallel spins. For $N=3$ (-0.522 V$<V_G=-0.502$ V), due to the circular symmetry of the potential in the *xy* plane, the electron has a definite *z* angular momentum component. This requirement is achieved by choosing the third electron orbital as[36] $|n_r,M,s\rangle=|0,1,\uparrow\rangle=\psi_1^{1(\uparrow)}+i\psi_1^{2(\uparrow)}$.[37] Here the spin symmetry is broken due to the odd number of electrons with two spin-up (↑) electrons and only one spin-down (↓) electron, which results in a larger ↑-xc (exchange and correlation) energy than the ↓-xc energy.

For $N=4$ (-0.502 V$<V_G=-0.467$ V), the fourth electron can either occupy the $|0,\pm1,\downarrow\rangle$ or $|0,-1,\uparrow\rangle$ state. These two configurations are shown in terms of the eigenspectrum as a function of the gate voltage at the $N=3\rightarrow4$ transition in Fig. 8. In the latter configuration, spin polarization, for the third and fourth electrons, lowers the total energy. This configuration is the favored one, as predicted by Hund's first rule in atomic physics.[1]

Addition energy measurements are the clearest way to show the shell structure in CVQD's. Figure 9 shows the variation of the addition energy with respect to the number of electrons *N*, as measured in Tarucha's experiment (dashed), and as computed in our simulations for three different confining potentials $\omega_1>\omega_2>\omega_3$ that correspond to 50-, 30-, and 20-meV conduction-band offsets ΔE_c between GaAs and $\mathrm{In}_x\mathrm{Ga}_{1-x}\mathrm{As}$, respectively. The band-offset variation is not unreasonable due to the fact that the GaAs conduction band edge with a doping density of $10^{17}/\mathrm{cm}^3$ is simply not well defined, and this can result in an impurity fluctuation at the well edge ($z=z_i$). Figure 9 shows very pronounced peak for $N=2$, 6, and 12 reminiscent of the shell structure in the experimental curve as well as in the simulation curves for $\omega=\omega_1$ and ω_2. For $\omega=\omega_3$, the confining potential is so weak that the shell structure begins to vanish. In this case, charging the second shell $(N=2)$ requires less energy than overcoming the repulsive energy generated by the first electron $(N=1)$, so that $E_a(1)<E_a(2)$. In the experimental curve, there are also secondary peaks for $N=4$, 9, and 16. These peaks are interpreted as the manifestation of Hund's rule with parallel spin alignment for a half-filled shell.[1–3] In the simulation curve, we clearly obtain the peaks at $N=4$ and 16, but not the peak at $N=9$, and have other secondary peaks at $N=8$, 10, 14, and 18.

If Hund's rule governs the filling of the second shell, then, necessarily, the addition energy spectrum will exhibit a peak at $N=4$ surrounded by two minima at $N=3$ and 5, as described in Sec. IV. Hence the third and fourth electrons, with parallel spins $(\uparrow)$, access the empty $|0,\pm 1,\uparrow\rangle$ orbitals, maximize the exchange interaction, and induce a minimum for $N=3$. For $N=4$, the fifth electron, occupying the $|0,1,\downarrow\rangle$ state, is the only $\downarrow$ electron in the second shell, with no additional exchange, i.e., $E_a(4)>E_a(3)$. For $N=5$, the sixth electron in the $|0,-1,\downarrow\rangle$ state induces exchange between the sixth and fifth electrons, which lowers $E_a(5)<E_a(4)$, leading to a peak for $N=4$.

The idea that the peak at $N=9$ is the manifestation of Hund's rule originates from the 2D circular oscillator model where the three states of the third shell are degenerate [Fig. 10(a)]. In this case, the filling sequence would be

$$2^{1/2}\rightarrow 2^{1}\rightarrow 0^{3/2}\rightarrow 2^{1}\rightarrow 2^{1/2}\rightarrow 0^{0} \tag{37}$$

leading to the configuration $1s^2 2p^4 3d^2 3s^1$, by adopting a terminology similar to atomic physics for representing the electronic orbitals. Here the $|1,0,\uparrow(\downarrow)\rangle$ (s-like) state is occupied before the $|0,\pm 2,\uparrow(\downarrow)\rangle$ (d-like) states to maximize the total orbital angular momentum. Consequently, the addition energy for $N=7$ and 8 are low, since the exchange interaction is maximized. In addition, $|1,0,\uparrow\rangle$ and $|0,\pm 2,\uparrow\rangle$ overlap weakly, which reduces the (repulsive) Hartree energy E_H. For $N=9$, the same argument as for $N=4$ applies, i.e., the tenth electron is the first $\downarrow$-electron of the third shell (no exchange-correlation) that sits on an already occupied orbital (large Hartree), producing a peak for $N=9$. However, it was demonstrated earlier (Sec. III B) that the accidental degeneracy between the $\varepsilon_2^{1,2}$ and ε_2^{3} is lifted in CVQD's. Hence, instead of the configuration and sequence shown in Fig. 10(a), the configuration shown in Fig. 10(b) with a separation $\Delta=\varepsilon_2^{3}-\varepsilon_2^{1,2}$ is achieved. For $\omega=\omega_1$, we obtain $\Delta\approx 1$ meV, and the energetically most favorable sequence is

$$2^{1/2}\rightarrow 0^{1}\rightarrow 2^{1/2}\rightarrow 0^{0}\rightarrow 0^{1/2}\rightarrow 0^{0}, \tag{38}$$

for which the electronic configuration for nine electrons is $1s^2 2p^4 3d^3$, with an incomplete spin alignment. Hence we see a peak at $N=8$ for the fulfillment of Hund's first rule in the lower subshell—a situation similar to the second shell with a peak at $N=4$, but also a peak at $N=10$ due to the increment of energy needed to reach the second subshell.

The reduction of ΔE_c, such as $\omega=\omega_2$, leads to a reduction of Δ from 1 to 0.5 meV. According to our simulations, when $\Delta>0.6$ meV, the third shell is also filled following the sequence (38). We point out that these values for Δ are in good agreement with experimental measurements.[1] When $\Delta<0.6$ meV, the third shell is filled with sequence (37), with three parallel spins predicted by Hund's rule, as represented in Fig. 10(c). This result has been reproduced many times in our simulations, for various structure sizes and various gate lengths.

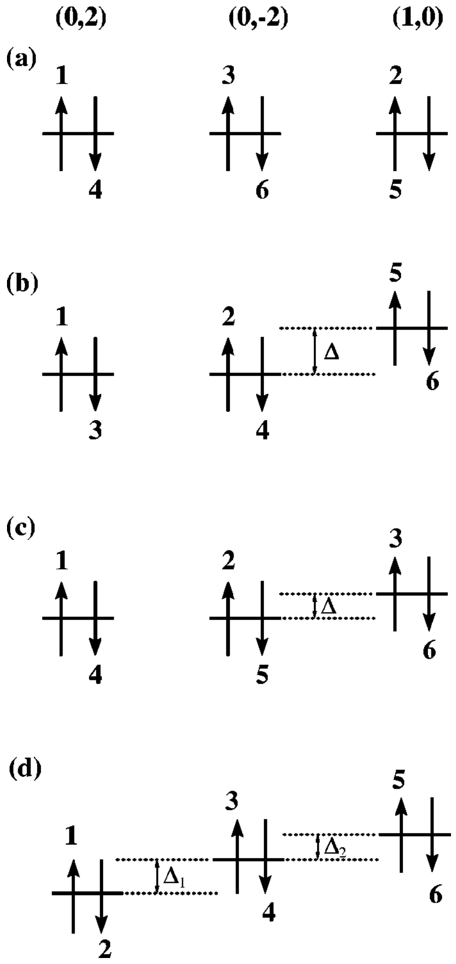

FIG. 10. Schematic possible sequences for the filling of the third shell (see Fig. 7 for realistic configurations) (a) In a 2D circular oscillator configuration, with three degenerate levels $(0,\pm 2)$ and $(1,0)$ and three spin alignments. (b) Large separation $\Delta>0.6$ meV between $(0,\pm 2)$ and $(1,0)$ leading to the filling sequence [Eq. (38)]. (c) Small separation $\Delta<0.6$ meV between $(0,\pm 2)$ and $(1,0)$ leading to the filling sequence [Eq. (37)]. (d) Total lifting of degeneracy with separations Δ_1 and Δ_2, respectively, leading to the usual pairing sequence $\uparrow\downarrow$ [Eq. (39)].

The ω_2 and ω_3 addition energy spectra in Fig. 9, although associated with a filling sequence governed by three parallel spin electrons at $N=9$ [Fig. 10(c)], exhibit a peak at $N=8$ instead of $N=9$. Placing the ninth electron on the s-state requires an additional energy Δ, which increases the addition energy for $N=8$. The tenth electron with antiparallel spin, although deprived from exchange interaction, falls on one of the d states, which lowers the addition energy for $N=9$. The addition energy for $N=10$ and 11 depends on the interplay

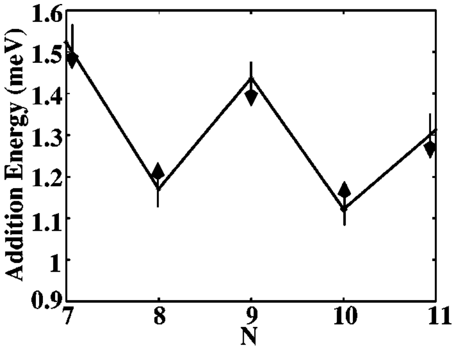

FIG. 11. Third shell addition energy spectrum of a quantum dot perturbed by a remote Coulombic impurity placed in the well, 2000 Å away from the center of the dot.

between exchange and Coulomb interaction for occupation of the second *d* state in the former, and the additional Δ for the latter in the *s* state. Hence the addition energy spectrum shows only one peak at $N=8$, with a magnitude which depends on the difference between Δ and E_{xc}.

Clearly, a peak at $N=9$ is not necessarily the signature of three spin alignment in the third shell. In fact, this situation was never achieved in our simulations. The failure of our model to reproduce the main experimental spectra is intriguing, but a key element is found in the addition energy at $N=7$: all the theoretical values are consistently lower than the value at $N=5$, whereas in the experimental data $E_a(7)>E_a(5)$, data which indicate weak exchange (or strong direct Coulomb) interaction between the two electrons on the degenerate *d* single-particle states. This is surprising, since in general DFT underestimates exchange interaction among electrons. This higher experimental value for $N=7$ can only be obtained with the lifting of the spatial degeneracy for the *d* states, as shown in Fig. 10(d). This can be caused by elliptic deviations from the circular shape of the dot, or by potential fluctuations arising from the long-range Coulomb interaction of ionized donors in the doped GaAs. For this purpose, simulations with a remote ionized donor placed in the quantum well, 1000 Å away from the center of the dot, have been performed. In this case, the third shell addition energy spectrum now corresponds to the usual pairing sequence

$$2^{1/2}\rightarrow 4^0\rightarrow 2^{1/2}\rightarrow 0^0\rightarrow 0^{1/2}\rightarrow 0^0, \tag{39}$$

which is shown in Fig. 11. The high value of $E_a(7)$ is due to the filling of the $|0,2,\uparrow\rangle$ state with an antiparallel spin electron. The peak at $N=9$ is due to a large Coulomb repulsion when the tenth electron sits on the $|0,-2,\uparrow\rangle$ state. The peak is surrounded by two minima at $N=8$ and 10 corresponding to a weak Coulomb repulsion when the ninth and eleventh electron occupy two empty states $|0,-2,\uparrow\rangle$ and $|1,0,\uparrow\rangle$. The pairing sequence [Eq. (39)] for the experimental third shell filling is validated by the data in Fig. 2 of Ref. 1, which clearly indicates a spin sequence with no spin alignment at midshell, although the addition energy spectrum exhibits a single peak at $N=9$.

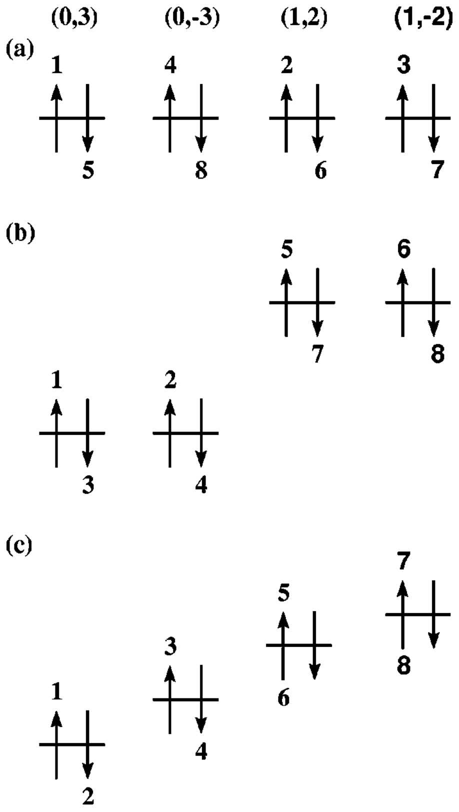

FIG. 12. Schematic possible sequences for the filling of the fourth shell. (a) In a 2D circular oscillator with four degenerate levels and four-spin alignment. (b) Separation between $(0,\pm 3)$ and $(1,\pm 2)$, leading to the formation of two twofold-degenerate subshells. (c) Total lifting of degeneracy leading to the usual pairing sequence $\uparrow\downarrow$.

It is now possible to suggest an interpretation for the peak at $N=16$ in the fourth shell. Since the accidental degeneracy between the $|0,\pm 3\rangle$ and $|1,\pm 2\rangle$ states is lifted in the CVQD's (see Sec. III B 1)—here the spacing between the two subshells is about 1.5 meV—a filling sequence predicting a four spin alignment up to $N=16$, as shown in Fig. 12(a), seems unlikely. As for $N=10$, in sequence (38), the peak at $N=16$ results from the excess energy required to access the second subshell in the fourth shell, as shown in Fig. 12(b). This figure also depicts the ordering sequence obtained in our DFT simulations, i.e.,

$$3^{1/2}\rightarrow 6^1\rightarrow 3^{1/2}\rightarrow 0^0\rightarrow 1^{1/2}\rightarrow 2^1\rightarrow 1^{1/2}\rightarrow 0^0, \tag{40}$$

for which the addition energy spectrum shows a jagged curve with alternative peaks and minima for even and odd numbers of electrons, respectively (Fig. 9). In sequence (40), the secondary peaks at $N=14$ and 18 result from the fulfillment of Hund's rule with two parallel spins at midoccupation within each subshell. In order to explain the experimental spectrum with a single peak at $N=16$,[1] we again consider the complete lifting of degeneracy caused by external static perturbations, as illustrated in Fig. 12(c). The minima at $N=14$ and 18 are then due to the filling of two empty states $|0,-3,\uparrow\rangle$ and $|1,-2,\uparrow\rangle$. The intermediate value at $N=13$, 15, and 19 result from the Coulomb repulsion due to the filling of the states

$|0,3,\downarrow\rangle$, $|0,-3,\downarrow\rangle$, and $|1,-2,\downarrow\rangle$, since their orbitals are very similar to $|0,3,\downarrow\rangle$, $|0,-3,\downarrow\rangle$, and $|1,-2,\downarrow\rangle$, respectively. The maximum at $N=16$, in this scenario, is also due to the energy increment needed to access the second subshell, made of the $|1,\pm 2\rangle$ orbitals.

VI. CONCLUSION

We have demonstrated that, in CVQD's, each shell degeneracy is lifted, even when the dot retains cylindrical symmetry, due to 3D device effects and electron-electron interaction in the dot. All these predictions are confirmed by numerical self-consistent simulations, and shed light on the electron charging sequence of CVQD's: far from being just the result of spatial degeneracy of electronic states within a single shell, the basic physical conditions for the different possible ways of filling electrons in the shells of a CVQD is a complicated interplay between symmetry breaking and Coulomb interaction between electrons. In particular, we have demonstrated that the third-shell filling sequence and addition energy spectrum depend on the magnitude of the level separation Δ. We have recently shown that these findings are in good agreement with experimental results.[38] Moreover, the existence of Hund's rule with shell filling of CVQD's is not necessarily related to the observation of specific peaks in the addition energy spectrum.

ACKNOWLEDGMENTS

This work was supported by NEDO and NSF Grant No. DESCARTES ECS-98-02730. One of us (P.M.) gratefully acknowledges the support of the Beckman Institute and A. Thean, for technical assistance. We are indebted to Professor S. Tarucha, Professor R. Martin, and Dr. G. Austing for valuable discussions.

---

[1] S. Tarucha, D. G. Austing, T. Honda, R. J. Van der Hage, and L. P. Kouwenhoven, Phys. Rev. Lett. **77**, 3613 (1996).

[2] S. Tarucha, D. G. Austing, and T. Honda, Jpn. J. Appl. Phys. **37**, 3917 (1997).

[3] L. P. Kouwenhoven, T. H. Oosterkamp, M. W. S. Danoesastro, M. Eto, D. G. Austing, T. Honda, and S. Tarucha, Science **278**, 1788 (1997).

[4] S. Tarucha, D. G. Austing, Y. Tokura, W. G. Van der Wiel, and L. P. Kouwenhoven, Phys. Rev. Lett. **84**, 2485 (2000).

[5] M. A. Kastner, Phys. Today **46**(1), 24 (1993).

[6] R. C. Ashoori *et al.*, Surf. Sci. **305**, 558 (1994).

[7] I.-H. Lee, V. Rao, R. M. Martin, and J.-P. Leburton, Phys. Rev. B **57**, 9035 (1998).

[8] J. Jefferson and W. Häusler, Molecular Physics Reports **17**, 81 (1997).

[9] J.-P. Leburton and S. Nagaraja, in *Optical Spectroscopy of Low Dimensional Semiconductor*, Vol. 344 of *NATO Advanced Study Institute, Series E: Title*, edited by G. Abstreiter *et al.* (Kluwer, Boston, 1997), pp. 235–256.

[10] C. Yannouleas and U. Landman, Phys. Rev. B **61**, 15895 (2000).

[11] F. Bolton, Phys. Rev. B **54**, 4780 (1996).

[12] F. Pederiva, C. Umrigar, and E. Lipparini, Phys. Rev. B **62**, 8120 (2000).

[13] J. Harting, O. Mülken, and P. Borrmann, Phys. Rev. B **62**, 10207 (2000).

[14] T. Ezaki, N. Mori, and C. Hamaguchi, Phys. Rev. B **56**, 6428 (1997).

[15] M. Rontani, F. Rossi, F. Manghi, and E. Molinari, Phys. Rev. B **59**, 10165 (1999).

[16] D. G. Austing, T. Honda, and S. Tarucha, Semicond. Sci. Technol. **11**, 388 (1996).

[17] S. Tarucha, D. G. Austing, and T. Honda, Superlattices Microstruct. **18**, 121 (1995).

[18] P. Matagne and J.-P. Leburton, Phys. Rev. B **65**, 155311 (2002).

[19] D. G. Austing, S. Sasaki, S. Tarucha, S. M. Reimann, M. Koskinen, and M. Manninen, Phys. Rev. B **60**, 11 514 (1999).

[20] B. Partoens and F. Peeters, Phys. Rev. Lett. **84**, 4433 (2000).

[21] W. de Heer, Rev. Mod. Phys. **65**, 611 (1993).

[22] R. Jones and O. Gunnarsson, Rev. Mod. Phys. **61**, 689 (1989).

[23] Y. Wang and Y. Chou, Appl. Phys. Lett. **63**, 2257 (1993).

[24] D. Jovanovic and J.-P. Leburton, Phys. Rev. B **49**, 7474 (1994).

[25] L. R. Fonseca, J. L. Jimenez, J.-P. Leburton, and R. M. Martin, Phys. Rev. B **57**, 4017 (1998).

[26] M. Macucci, K. Hess, and G. Iafrate, Phys. Rev. B **48**, 17354 (1993).

[27] M. Stopa, Phys. Rev. B **54**, 13767 (1996).

[28] The agreement with 2D QMC simulations is very good up to $N=12$. However, for $N=4$, the QMC simulations (Refs. 12 and 13) give the singlet state $|LS\rangle=|00\rangle$ as the lowest-energy state as opposed to the triplet state $|01\rangle$ obtained in DFT, which is in agreement with experiments (Refs. 1–4). This emphasizes the importance of the third dimension in realistically modeling the confining potential in the dot.

[29] P. Matagne, J.-P. Leburton, J. Destine, and G. Cantraine, Comput. Modeling Eng. Sci. **1**, 1 (2000).

[30] R. Grant, J. Waldrop, S. Kowalczyk, and E. Kraut, J. Vac. Sci. Technol. **19**, 477 (1981).

[31] J. Best, Appl. Phys. Lett. **34**, 522 (1979).

[32] J. Slater, Adv. Quantum Chem. **6**, 1 (1972).

[33] K. K. Likharev, Proc. IEEE **87**, 606 (1999).

[34] D. Averin and K. K. Likharev, J. Low Temp. Phys. **62**, 345 (1986).

[35] S. Nagaraja *et al.*, Phys. Rev. B **56**, 15752 (1997).

[36] *Elements de Mecanique Ondulatoire*, edited by W. Heitler (Bibliotheque Scientifique Internationale, Paris, 1964).

[37] The choice of a particular spin as well as the sign of the angular quantum number M is, of course, arbitrary. Similarly, for the third shell, we choose $|0,\pm 2\rangle=\psi_2^1\pm i\psi_2^2$ and $|1,0\rangle=\psi_2^3$. For the fourth shell, $|0,\pm 3\rangle=\psi_3^1\pm i\psi_3^2$ and $|1,\pm 2\rangle=\psi_4^1\pm i\psi_4^2$.

[38] P. Matagne, J.-P. Leburton, D. Austing, and S. Tarucha, Phys. Rev. B **65**, 085325 (2002).